



Y. Mohammad Hashemi · M. Kadkhodaei  · M. Salehan

Fully coupled thermomechanical modeling of shape memory alloys under multiaxial loadings and implementation by finite element method

Received: 8 April 2019 / Accepted: 7 August 2019 / Published online: 16 August 2019
© Springer-Verlag GmbH Germany, part of Springer Nature 2019

Abstract Different constitutive models along with various numerical implementation approaches have been proposed for shape memory alloys (SMAs) in the last decades. Since 1-D models are only suitable for particular geometries and loading types, due to the broad variety of SMA components in smart structures, 3-D rate-dependent modeling of SMAs is a necessity. In the present research, a fully coupled rate-dependent model to study thermomechanical response of shape memory alloys under multiaxial loadings is presented. The model is implemented into ABAQUS commercial finite element package by developing a user-defined material subroutine. Most of the available works are limited to just mechanical loadings and/or simple geometries, but the current model is able to simulate both shape memory effect and pseudoelasticity. Furthermore, it is capable of being applied to any geometry undergoing thermal/mechanical cycling under a wide range of strain rates spanning quasi-static to high-rate conditions. The obtained numerical results by the model are validated by experimental, analytical, and numerical findings of available three-dimensional case studies in the literature. The predicted results by the current model are shown to be in good agreement with the findings of previous investigations.

Keywords Shape memory alloy · Multiaxial loading · Thermomechanical model · Three-dimensional model · Finite element method · UMAT

1 Introduction

Shape memory alloys (SMAs), which are known as a category of smart materials, have special characteristics including shape memory effect (SME) and pseudoelasticity (PE) owing to their martensitic phase transformation. These characteristics have attracted the attention of researchers to employ them in customary as well as high-tech areas comprising aerospace, automotive, robotics, and biomechanics [1]. Shape memory effect is the ability to recover deformed shape into a predefined one by heating up to austenite transformation temperature. On the other hand, pseudoelasticity, which is observed at high temperatures, accompanies large amounts of recoverable strains up to 8.5% without heating requirements [1]. These particular behaviors make shape memory alloys attractive candidates in a wide range of applications from areas where other smart materials are applicable (such as piezoelectric materials to control sound radiation and vibrations [2–5]) to cases in which hysteresis and the consequent damping [6] or self-healing [7] in these alloys are employed. An interesting application of SMAs may follow the key idea of metamaterials that is to design a material starting from the main behavior which one wants to be attained and to propose a particular substructure which is able to accomplish this goal [8–10]. From the viewpoint of thermomechanical response, the existence of hysteresis in SMAs

Communicated by Victor Eremeyev and Holm Altenbach.

Y. M. Hashemi · M. Kadkhodaei (✉) · M. Salehan
Department of Mechanical Engineering, Isfahan University of Technology, Isfahan 84156-83111, Iran
E-mail: kadkhodaei@cc.iut.ac.ir

leads their behaviors to be rate-dependent. There are models for hysteretic phenomena in both rate-independent and rate-dependent behaviors of typical materials [11–13].

Various configurations of SMAs are used in engineering applications. Since SMA wires, springs, foils, and strips are commonly subjected to uniaxial loadings under small amounts of deformation, they are mostly simulated by one-dimensional models. However, either applying large amounts of deformation on the above-mentioned configurations or employing complex geometries such as endodontic files reveals the necessity of employing multi-axial models. To investigate plates and shells made of SMAs or other materials undergoing phase transitions, Eremeyev and Pietraszkiewicz [14] found 2-D shell relations from the variational principle of the stationary total potential energy. Based on an extension of this approach [15], two-dimensional thermomechanics of shells undergoing diffusionless, displacive phase transitions of martensitic type for shell materials was developed [16]. From the integral forms of balance laws of linear momentum, angular momentum, and energy as well as the entropy inequality, Eremeyev and Pietraszkiewicz [17] obtained the local static balance equations along the curvilinear phase interface. They discussed general forms of the constitutive equations for thermoelastic and thermoviscoelastic shells. They also derived the thermodynamic condition allowing one to determine the interface position on the deformed shell midsurface. These 2-D models can capture some peculiarities of phase transitions like the ones in a full 2-D analysis; however, they are approximated models and are shown to be valid for certain assumptions [18].

Early 3-D models of SMAs were presented for quasi-static circumstances which consider the applied strain rate to be low enough so that the temperature variations become negligible. Boyd and Lagoudas [19] presented a model for multi-axial loading of SMAs by employing a four-lined phase diagram. Lim and McDowell [20] found that proposed SMA models for proportional loadings are not necessarily appropriate to be used for non-proportional ones. Subsequently, Peng et al. [21] presented the concept of generalized effective stress which was inspired from von Mises equivalent stress. However, coefficients of the proposed generalized effective stress were material-dependent. Bouvet et al. [22] proposed a model for proportional as well as nonproportional loadings of pseudoelastic SMAs by introducing the phenomenon of phase transformation surfaces. Simulating the response of an SMA component exposed to a multi-axial loading can be conducted by considering different variants of martensite, which leads to considerable time-consuming and numerically complicated models [23,24]. Kadkhodaei et al. [25] proposed a model for multi-axial nonproportional loadings under quasi-static circumstances by applying the so-called microplane theory to SMAs. Their approach has been shown to be simpler for numerical implementations and to be extensible for addressing various details in the responses of shape memory alloys [26–29]. Three-dimensional models are also beneficial for designing/studying functionally graded shape memory alloys. Xue et al. [30] investigated the amounts of stress in a functionally graded SMA cylinder subjected to inner and outer pressures as well as thermal gradient using finite element analysis.

Since cyclic loading of SMAs is accompanied by energy dissipation and temperature variations, the applied stress–strain rate greatly influences the stress–strain response of an SMA component. Many attempts have been made to propose a thermomechanical model for an SMA wire subjected to cyclic loadings [31–34]. Morin et al. [34] presented a rate-dependent model to determine the stabilized dissipated energy in stress–strain response of an SMA wire. Alipour et al. [35] implemented the uniaxial model of Kadkhodaei et al. [33] into ABAQUS finite element software to enable a fully coupled thermomechanical model to be utilized in finite element simulation of smart structures containing SMA wires. Toward generalizing 1-D models to 3-D ones, Boyd and Lagoudas [19] presented a multi-axial rate-dependent model by proposing a correlated Gibbs free energy. Morin et al. [36] simulated the mechanical response of SMA cylinders surrounded by different environments of air as well as water under various strain rates by a three-dimensional thermomechanical model. However, capabilities of their model were investigated just for uniaxial tensile loadings. Mirzaeifar et al. [37] employed the Gibbs free energy as the thermodynamic potential, proposed a 3-D rate-dependent model, and studied the mechanical response of SMA wires and bars subjected to tensile loadings under different convection conditions. Although their model was presented in three dimensions, their studies were conducted by a reduced one-dimensional problem using finite difference method. In another investigation, Mirzaeifar et al. [38] reduced their three-dimensional model to one-dimensional pure torsion and studied mechanical response of circular bars under various ambient conditions. Such numerical implementations mostly confine the formulation to a specific geometry or cycling type, i.e., mechanical or thermal loading. Andani et al. [39] investigated the thermomechanical response of pseudoelastic bars subjected to tension–torsion loading. Although they employed a three-dimensional rate-dependent model, the formulation was simplified for 2-D rate-dependent loadings. They also presented a correlation for free heat convection of an SMA bar and validated their approach by empirical findings [39]. Andani et al. [40] further presented general equivalent stress and strain to investigate the pseudoelastic response of SMAs under nonproportional tension–torsion loadings. As

stated above, although most of the available models have been derived for multiaxial loadings, they have been either solved intrinsically like one-dimensional cases or proposed particularly for the pseudoelasticity response. Moreover, their numerical implementation method has been limited to a specified geometry. On the other hand, investigations in the literature are mostly narrowed to mechanical loadings, and less attention has been paid to thermal cycling of SMAs.

In this paper, a three-dimensional rate-dependent model for shape memory alloys is presented in a continuum framework by extending Kadkhodaei's formulation [33] for 3-D loadings. Furthermore, a user-defined material subroutine (UMAT) is provided by which the formulation is implemented into ABAQUS commercial finite element package. It is shown that the model is able to simulate shape memory effect as well as pseudoelasticity under different strain rates spanning quasi-static to high-rate loadings. Although most of the available works are limited to specified geometries and/or loading types, the presented approach in this work is capable of modeling SMA components with any geometry and boundary conditions under both mechanical and thermal loadings. The obtained numerical results for different geometries and loading types including tensile loading of SMA wires/bars, uniaxial loading of SMA thin-walled tubes, multiaxial loading of thin-walled tubes, and axial loading of SMA helical springs are validated against available experimental, analytical, and numerical findings reported in former studies.

2 Modeling

Total strain tensor of SMAs (ϵ) can be decomposed into elastic (ϵ^e) and transformation (ϵ^{tr}) parts:

$$\epsilon = \epsilon^e + \epsilon^{tr} \quad (1)$$

where the elastic tensor is defined by:

$$\epsilon^e = \mathbf{C}^{-1} : \boldsymbol{\sigma} = \mathbf{S} : \boldsymbol{\sigma} \quad (2)$$

in which \mathbf{C} is the stiffness tensor, \mathbf{S} is the compliance tensor, and $\boldsymbol{\sigma}$ is the stress tensor. According to Reuss scheme, the Young's modulus is defined by Eq. (3):

$$\frac{1}{E} = \frac{\xi}{E_M} + \frac{1-\xi}{E_A} \quad (3)$$

where E_M , E_A , and ξ are the Young's modulus of pure martensite, the Young's modulus of pure austenite, and martensite volume fraction, respectively. Martensite volume fraction, which comprises stress- (ξ_s) and temperature-induced (ξ_T) portions, is calculated for different regions of a stress-temperature phase diagram by kinetic evolution functions [41,42]:

$$\xi = \xi_T + \xi_s \quad (4)$$

Derivation of the Young's modulus with respect to martensite volume fraction yields Eq. (5):

$$\frac{dE}{d\xi} = E^2(\xi) \left(\frac{1}{E_A} - \frac{1}{E_M} \right) \quad (5)$$

Thus, one may consider the following relations:

$$\mathbf{C} = E\mathbf{C}' \quad (6)$$

$$\mathbf{S} = \frac{\mathbf{S}'}{E} \quad (7)$$

Derivatives of the stiffness and compliance tensors with respect to time are expressed by the following equations:

$$\dot{\mathbf{C}} = \frac{dE}{d\xi} \mathbf{C}' \dot{\xi} \quad (8)$$

$$\dot{\mathbf{S}} = \left(\frac{1}{E_M} - \frac{1}{E_A} \right) \mathbf{S}' \dot{\xi} \quad (9)$$

$$\dot{\mathbf{C}} = -\mathbf{C} : \dot{\mathbf{S}} : \mathbf{C} \quad (10)$$

On the other hand, the transformation strain tensor in Eq. (1) can be expressed by:

$$\boldsymbol{\epsilon}^{\text{tr}} = \boldsymbol{\epsilon}^* \xi_s \quad (11)$$

In this correlation, $\boldsymbol{\epsilon}^*$ is the maximum recoverable strain tensor in which the constant volume limitation upon martensitic transformation is satisfied. Maximum recoverable strain tensor is defined for forward as well as backward transformation by:

$$\boldsymbol{\epsilon}^* = \frac{3}{2} \frac{\boldsymbol{\sigma}'}{\bar{\sigma}} \boldsymbol{\epsilon}^* \quad (12)$$

where $\boldsymbol{\epsilon}^*$, $\boldsymbol{\sigma}'$, and $\bar{\sigma}$ are the maximum recoverable strain in simple tensile test, the deviatoric stress tensor, and von Mises effective stress, respectively. The deviatoric stress tensor and effective stress are calculated by the equations below:

$$\boldsymbol{\sigma}' = \boldsymbol{\sigma} - \frac{1}{3} \text{Tr}(\boldsymbol{\sigma}) \mathbf{I} \quad (13)$$

$$\bar{\sigma} = \sqrt{\frac{3}{2} \boldsymbol{\sigma}' : \boldsymbol{\sigma}'} \quad (14)$$

Since the evolution functions of martensite volume fraction are defined for axial loadings, the martensite volume fraction is calculated in multiaxial loadings based on the value of effective stress. In order to consider rate dependency in SMA models, appropriate energy functions are needed to be applied along with the constitutive equations. In this work, the Helmholtz free energy is considered as:

$$\psi = \frac{\boldsymbol{\epsilon}^e : \mathbf{C} : \boldsymbol{\epsilon}^e}{2\rho} - \frac{\mathbf{C} : \boldsymbol{\alpha} : \boldsymbol{\epsilon}^e (T - T_0)}{\rho} + C \left((T - T_0) - T \ln \left(\frac{T}{T_0} \right) \right) + \frac{\lambda}{T^*} (T - T^*) \xi \quad (15)$$

in which ρ , $\boldsymbol{\alpha}$, T_0 , T^* , λ , and C are mass density, thermal expansion tensor, reference temperature, phase equilibrium temperature, latent heat of martensitic transformation, and specific heat, respectively. According to Eq. (15), specific entropy (η) and specific internal energy (u) are defined by the following relations:

$$\eta = -\frac{\partial \psi}{\partial T} = \frac{\mathbf{C} : \boldsymbol{\alpha} : \boldsymbol{\epsilon}^e}{\rho} + C \ln \left(\frac{T}{T_0} \right) - \frac{\lambda}{T^*} \xi \quad (16)$$

$$u = \psi + T\eta = \frac{\boldsymbol{\epsilon}^e : \mathbf{C} : \boldsymbol{\epsilon}^e}{2\rho} + \frac{\mathbf{C} : \boldsymbol{\alpha} : \boldsymbol{\epsilon}^e T_0}{\rho} + C(T - T_0) - \lambda \xi \quad (17)$$

Ignoring the second term in Eq. (17) based on small contribution of the thermal expansion [35], \dot{u} is expressed as

$$\dot{u} = \frac{\boldsymbol{\epsilon}^e : \mathbf{C} : \dot{\boldsymbol{\epsilon}}^e}{\rho} + \frac{\boldsymbol{\epsilon}^e : \dot{\mathbf{C}} : \boldsymbol{\epsilon}^e}{2\rho} + C\dot{T} - \lambda \dot{\xi} \quad (18)$$

On the other hand, the first law of thermodynamics is:

$$\rho \dot{u} + \nabla \cdot \mathbf{q} - \boldsymbol{\sigma} : \dot{\boldsymbol{\epsilon}} = 0 \quad (19)$$

Substituting the values of $\dot{\boldsymbol{\epsilon}}^e$ and $\boldsymbol{\epsilon}^e$ into Eq. (18), \dot{u} and the first law of thermodynamics are determined by Eqs. (20) and (21):

$$\dot{u} = \frac{\mathbf{S} : \boldsymbol{\sigma} : \mathbf{C} : (\dot{\boldsymbol{\epsilon}} - \dot{\boldsymbol{\epsilon}}^* \xi_s - \boldsymbol{\epsilon}^* \dot{\xi}_s)}{\rho} - \frac{\mathbf{S} : \boldsymbol{\sigma} : \dot{\mathbf{S}} : \mathbf{C} : \boldsymbol{\sigma}}{2\rho} + C\dot{T} - \lambda \dot{\xi} \quad (20)$$

$$\left[-\left(\frac{1}{E_M} - \frac{1}{E_A} \right) \frac{\boldsymbol{\sigma} : \mathbf{S}' : \boldsymbol{\sigma}}{2} - \rho \lambda \right] \dot{\xi} + \boldsymbol{\sigma} : (-\dot{\boldsymbol{\epsilon}}^* \xi_s - \boldsymbol{\epsilon}^* \dot{\xi}_s) + \rho C \dot{T} + \nabla \cdot \mathbf{q} = 0 \quad (21)$$

The derivatives of maximum recoverable strain tensor, stress-induced, and temperature-induced martensite volume fraction with respect to time in Eq. (21) are calculated by Eqs. (22) and (23):

$$\dot{\boldsymbol{\epsilon}}^* = \frac{d\boldsymbol{\epsilon}^*}{d\boldsymbol{\sigma}} \frac{\partial \boldsymbol{\sigma}}{\partial \boldsymbol{\epsilon}} \dot{\boldsymbol{\epsilon}} \quad (22)$$

$$\dot{\xi}_{s,t} = \frac{\partial \xi_{s,t}}{\partial \bar{\sigma}} \frac{d\bar{\sigma}}{d\sigma} \frac{\partial \sigma}{\partial \epsilon} \dot{\epsilon} + \frac{\partial \xi_{s,t}}{\partial T} \dot{T} \quad (23)$$

By neglecting the associated term with elastic deformations in Helmholtz free energy (Eq. (15)) due to its small contribution [35], the first law of thermodynamics is obtained as:

$$-\rho \lambda \dot{\xi} - \sigma : \dot{\epsilon} + \rho C \dot{T} + \nabla \cdot \mathbf{q} = 0 \quad (24)$$

Simultaneous solution of the first law of thermodynamics and the constitutive equation (Eq. 1) gives the instantaneous amounts of temperature, stress, and strain variations of an SMA under any thermomechanical loading.

3 Numerical implementation

ABAQUS finite element commercial package was employed for numerical implementation of the presented model. The material behavior was defined by developing a user-defined material subroutine (UMAT). The first law of thermodynamics is contributed in the UMAT to a variable, named RPL, which corresponds to the volumetric heat generation per unit time [43]. Therefore, according to Eq. (24), the RPL is stated for SMAs by:

$$\text{RPL} = \rho \lambda \dot{\xi} + \sigma : \dot{\epsilon} \quad (25)$$

Table 1 details the incremental computation algorithm of the developed UMAT. In this table, M_s , M_f , A_s , A_f , C_A , C_M , σ_s^{cr} , σ_f^{cr} , σ_s^{AM} , σ_f^{AM} , σ_s^{MA} , and σ_f^{MA} denote the start and finish temperatures of martensite transformation, the start and finish temperatures of austenite transformation, the slope of backward transformation strip, the slope of forward transformation strip, the start and finish stresses of detwinning, the start and finish stresses of forward transformation, and the start and finish stresses of backward transformation, respectively. Figure 1 illustrates schematic representation of a phase diagram in which the above-mentioned material parameters are depicted.

Since shape memory alloys have rather complex thermomechanical behaviors, solution of their nonlinear constitutive equations may accompany convergence difficulties. One way to optimize convergence in numerical implementation of the developed approach is to use a stress-based algorithm since the evolution rules of the martensite volume fraction are direct functions of stress. Moreover, the techniques of model order reduction may be beneficial in this regard.

4 Results and discussions

In this section, numerical and empirical findings in the literature under quasi-static as well as rate-dependent circumstances are employed to verify the presented model in different loading types. As the first case study, the obtained finite element results by the current model for quasi-static loadings are validated by 1-D FE results of Alipour et al. [35], who implemented the uniaxial model of SMA wires into ABAQUS finite element software. It is worth mentioning that 3-D geometry of a wire is utilized in the present results. Figure 2 shows this comparison for the pseudoelastic response of an SMA wire subjected to tensile loading using the material parameters of Table 2, and Fig. 3 compares the results for quasiplastic response where detwinning occurs. In Figs. 2 and 3, the results are reported at the temperatures of 55 °C and 25 °C, respectively. In Fig. 4, a constant stress of 140 MPa is applied and the wire is then subjected to thermal cycling between the temperatures of 5 °C and 60 °C. The illustrated curves provide the SMA response within the so-called dual transformation region [42]. Figures 2, 3, 4 show that the presented 3-D model can successfully investigate 1-D quasi-static responses of an SMA.

For the next verification step, the given material parameters in Table 3 are utilized to evaluate the ability of the presented formulation in considering the influences of strain rate on typical 1-D response of an SMA wire. Figures 5 and 6 illustrate the temperature–strain and stress–strain responses of an NiTi wire at two strain rates of 0.0005 s⁻¹, and 0.01 s⁻¹, respectively. Maximum errors of 0.3% and 0.1% are seen in the predicted temperatures at the strain rates of 0.01 s⁻¹ and 0.0005 s⁻¹, respectively, compared to the results obtained by Kadkhodaei et al [33]. As expected, the developed model predicts more pronounced variations in the temperature of an SMA specimen at higher strain rates.

Table 1 UMAT algorithm for three-dimensional loading of SMAs

Input: ϵ_n^{ij} , $d\epsilon_n^{ij}$, σ_n^{ij} , T_n , dT

Output: σ_{n+1}^{ij} , $\frac{d\sigma_{n+1}^{ij}}{d\epsilon_{n+1}^{kl}}$, **RPL**, $\frac{d\sigma_{n+1}^{kl}}{dT}$, $\frac{dRPL}{d\epsilon_{n+1}^{ij}}$, $\frac{dRPL}{dT}$

Loading

1. Calculate Critical Stresses: $\sigma_s^{AM} = \sigma_s^{cr} + C_M(T_{n+1} - M_s)$,

$$\sigma_f^{AM} = \sigma_f^{cr} + C_M(T_{n+1} - M_s) \quad (\text{for } T_{n+1} > M_s)$$

$$\sigma_s^{AM} = \sigma_s^{cr}, \quad \sigma_f^{AM} = \sigma_f^{cr} \quad (\text{for } T_{n+1} < M_s)$$

2. if $\sigma < \sigma_s^{AM}$ Before Transformation

$$-\xi = \xi_0; \text{ Calculate Young's Modulus}; \sigma_{n+1}^{ij} = \sigma_n^{ij} + C^{ijkl}d\epsilon^{kl};$$

3. if $\sigma_s^{AM} < \sigma < \sigma_f^{AM}$ Within Transformation

$$-\text{Suppose that } \sigma_{n+1}^{ij} = \sigma_n^{ij} \text{ (the initial value for stress)}$$

Start Loop"

$$-\text{Calculate } \xi; \text{ Calculate Young's Modulus}; \text{ Calculate } \frac{d\sigma_{n+1}^{ij}}{d\epsilon_{n+1}^{kl}};$$

$$-\text{Residual}^{ij} = (S^{ijkl}\sigma^{kl} + \epsilon^{*ij}\xi_s) - \epsilon^{ij}$$

-if $\text{Residual}^{ij} < \text{Tolerance}$

$$-\text{Calculate: RPL}, \frac{d\sigma_{n+1}^{kl}}{dT}, \frac{dRPL}{d\epsilon_{n+1}^{ij}}, \frac{dRPL}{dT}; \text{Exit Loop};$$

-else

$$-\text{Correct Stress: } \sigma_{n+1}^{ij} = \sigma_{n+1}^{ij} + \frac{d\sigma_{n+1}^{ij}}{d\epsilon_{n+1}^{kl}} * \text{Residual}^{kl}$$

-Go to Loop Start

End Loop

4. if $\sigma > \sigma_f^{AM}$ After Transformation

-Similar to 2nd Step of Loading

Unloading

1. Calculate Critical Stresses: $\sigma_s^{MA} = C_A(T_{n+1} - A_s)$, $\sigma_f^{MA} = C_A(T_{n+1} - A_f)$

$$\text{if } \sigma_s^{MA} < 0 \text{ then } \sigma_s^{MA} = 0$$

$$\text{if } \sigma_f^{MA} < 0 \text{ then } \sigma_f^{MA} = 0$$

2. if $\sigma > \sigma_s^{MA}$ Before Transformation

- Similar to 2nd Step of Loading

3. if $\sigma_f^{MA} < \sigma < \sigma_s^{MA}$ Within Transformation

- Similar to 3rd Step of Loading

4. if $\sigma < \sigma_f^{MA}$ After Transformation

- Similar to 4th Step of Loading

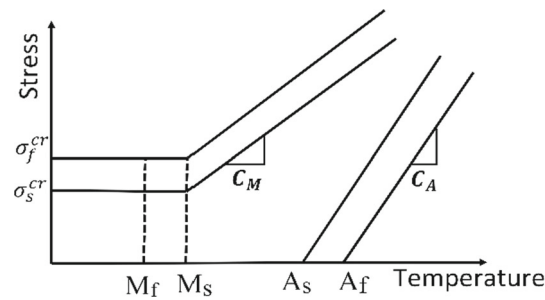


Fig. 1 Stress–temperature phase diagram of an SMA

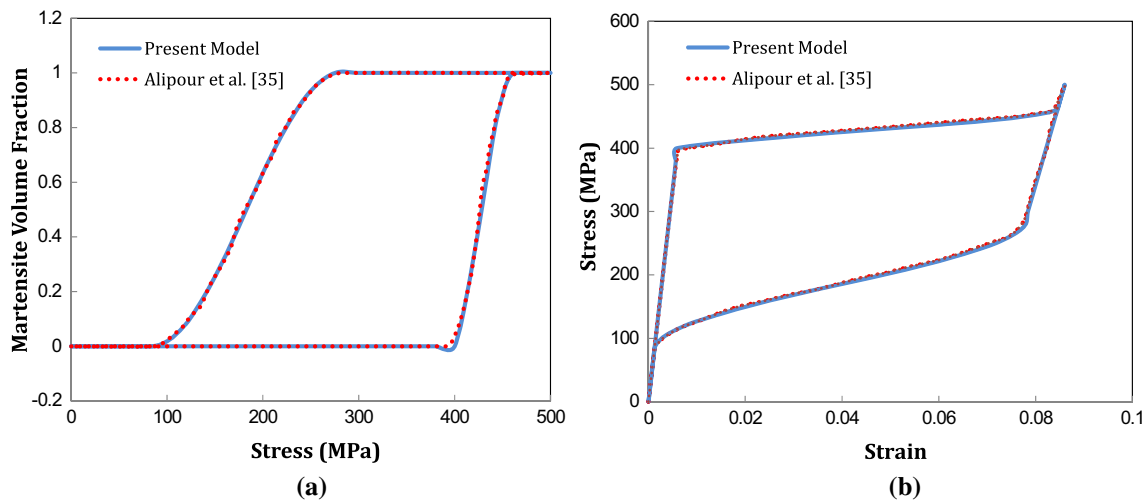


Fig. 2 Comparison between the results of Alipour et al. [35] and the current model for an SMA wire subjected to tension at 55 °C: **a** variation in martensite volume fraction and **b** stress–strain response

Table 2 Utilized material parameters for Figs. 2, 3, 4 [35]

M_f (°C)	M_s (°C)	A_s (°C)	A_f (°C)	C_A (MPa/°C)	C_M (MPa/°C)
9	18.4	34.5	49	13.8	8
σ_f^{cr} (MPa)	σ_s^{cr} (MPa)	E_A (GPa)	E_M (GPa)	ϵ^*	
170	100	67	26.3	0.067	

Mechanical response of an SMA can be affected by either geometrical changes in its configuration or application of large amounts of deformation. Since these effects are mostly neglected in numerical models, it is beneficial to employ a 3-D model using a finite element software even for simple geometries such as bars. Hence, numerical and experimental results of Mirzaeifar et al. [37] are utilized to study the stress–temperature and stress–strain responses of an SMA bar with 12.7 mm diameter subjected to tensile loading as shown in Fig. 7. The applied strain rate, initial temperature, and ambient temperature are 0.001 s^{-1} , 304.6 K, and 301 K, respectively. Figure 7 illustrates that the FE simulation results by presented 3-D model are in good agreements with empirical as well as analytical results of Mirzaeifar et al. [37]. Stress distribution in the cross section of thin wires is usually considered to be uniform; however, in the case of SMA bars, according to temperature distribution in the cross section, this assumption may be influenced by size effect and the ambient/loading conditions [37]. Implementation of the current model into ABAQUS provides the ability of simulating SMA bars with any cross section considering the above-mentioned effects. On the other hand, stress concentration induced by grippers for an SMA bar subjected to tension is another issue which can lead stress distribution of an SMA bar to be nonuniform, and such details are able to be taken into account by the current model.

To verify the model in torsion, two common geometries of bars and thin-walled tubes can be employed in the finite element simulations. SMA thin-walled tubes demonstrate uniform stress distribution under torsion

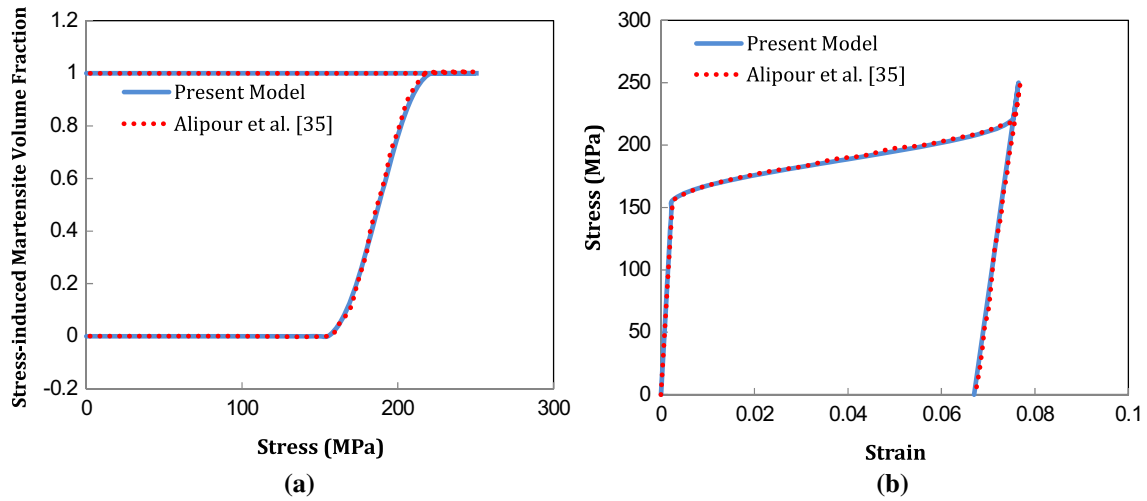


Fig. 3 Comparison between the results of Alipour et al. [35] and the current model for an SMA wire subjected to tension at 25 °C: **a** variation in stress-induced martensite volume fraction and **b** stress–strain response

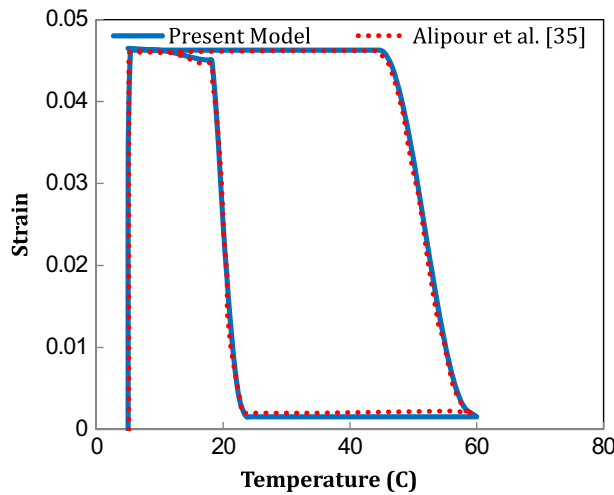


Fig. 4 Comparison between the predicted strain–temperature response by the current model and the numerical results of Alipour et al. [35] for an SMA wire subjected to thermal cycling in the dual transformation region

Table 3 Utilized material parameters for rate-dependent simulation of an SMA wire (Figs. 5 and 6) [33]

M_f (°C)	M_s (°C)	A_s (°C)	A_f (°C)	C_A (MPa/°C)	C_M (MPa/°C)	ϵ^*
42	55	52	65	8	12	0.067
E_A (GPa)	E_M (GPa)	σ_f^{cr} (MPa)	σ_s^{cr} (MPa)	ρ (kg/m ³)	C (J/kg.K)	λ (J/kg)
45	20.3	172	138	6500	600	5000

at their cross section and also a high potential in convective heat transfer in comparison with SMA bars. Therefore, they are preferred over solid bars for studying torsion. Predictions of the proposed model for variations in temperature and stress with respect to strain in an SMA tube are compared with Mirzaeifar’s findings [38] in Fig. 8. Temperature and equivalent strain rate are 287 K and 0.0005 s⁻¹, respectively. For details of the employed material parameters to obtain Fig. 8, readers may refer to Mirzaeifar’s papers [37,38]. To fulfill the model verification in the case study of torsion, the findings of Andani et al. [39] under the shear strain rate of 0.004 s⁻¹ are also utilized as shown in Fig. 9. In addition to torsional loadings of SMA tubes, due to the importance of thin-walled tubes in multiaxial loadings, the tensile loading of this configuration

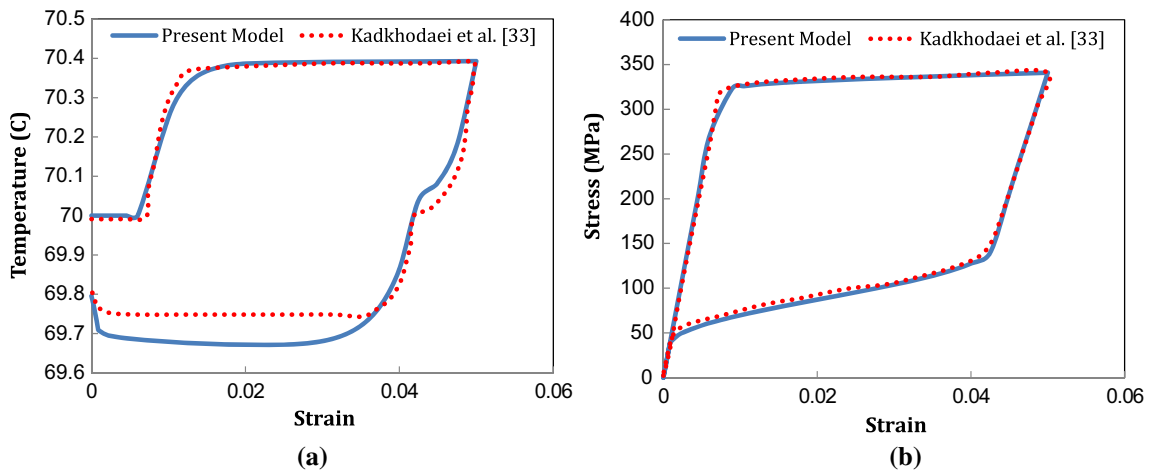


Fig. 5 **a** Temperature variation and **b** stress–strain response simulated by Kadkhodaei’s model [33] and current formulation for an NiTi wire subjected to tensile loading under the strain rate of 0.0005 s^{-1}

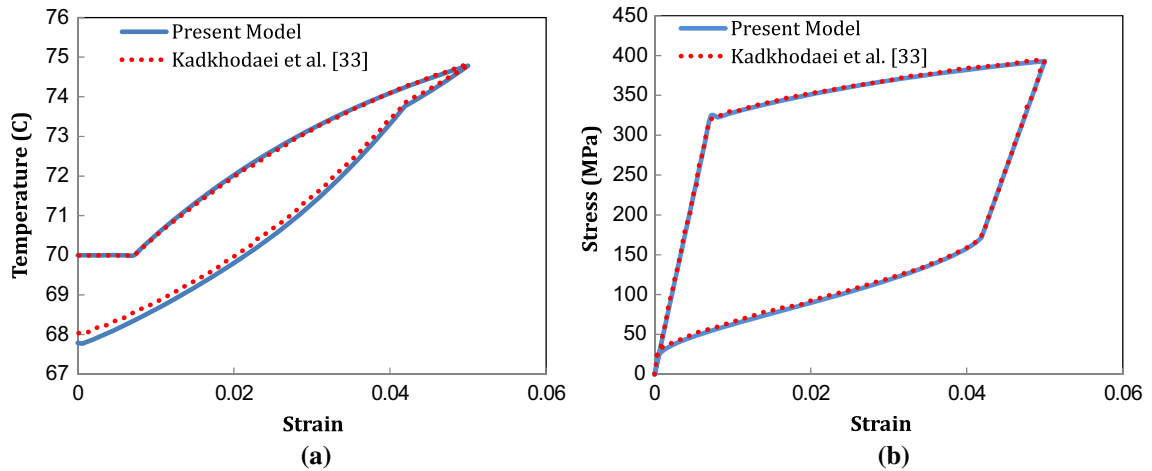


Fig. 6 **a** Temperature variation and **b** stress–strain response simulated by Kadkhodaei’s model [33] and current formulation for an NiTi wire subjected to tensile loading under the strain rate of 0.01 s^{-1}

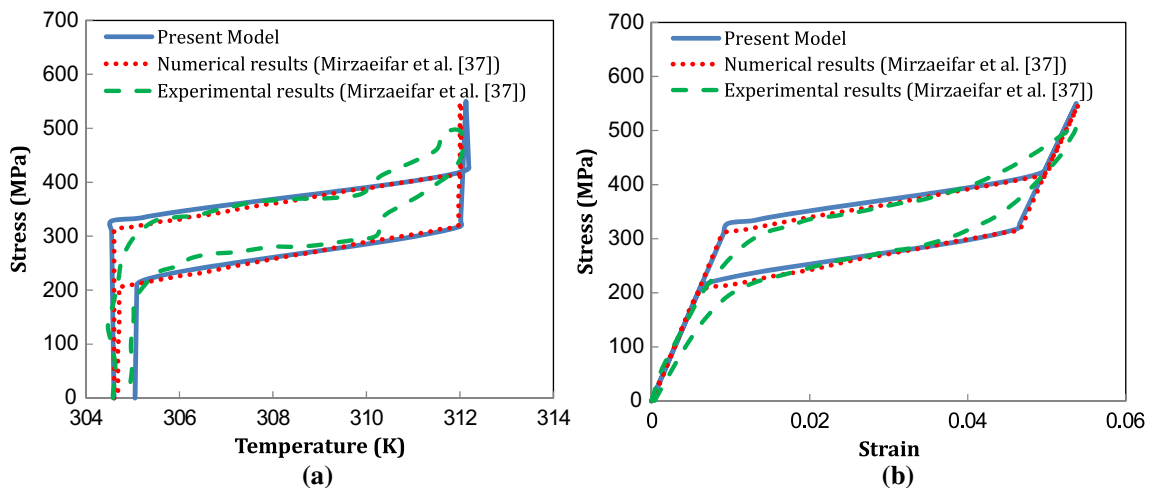


Fig. 7 Comparison of predicted results by the current model with experimental and numerical data of Mirzaeifar et al. [37] for tensile loading of an SMA bar: **a** stress–temperature response and **b** stress–strain response

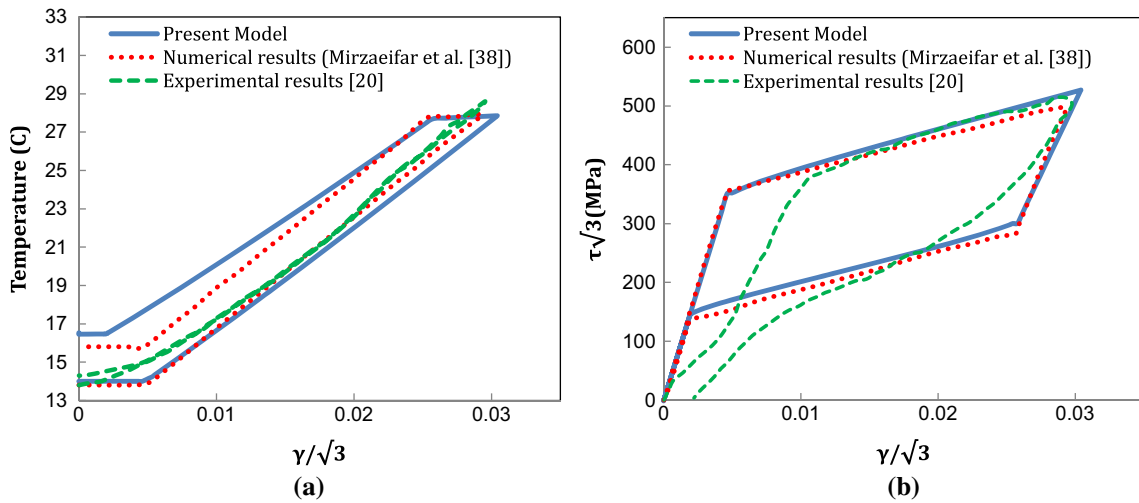


Fig. 8 Comparison of the predicted results by the current model with available numerical and experimental findings for a thin-walled SMA tube subjected to torsion: **a** temperature-equivalent strain response and **b** equivalent stress-equivalent strain response

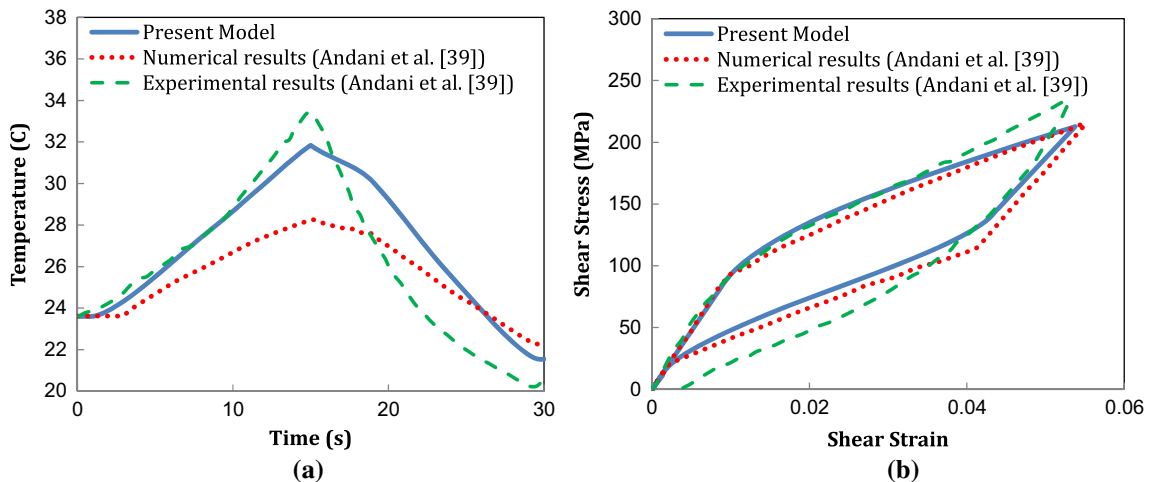


Fig. 9 Comparison of predicted results by the current model with numerical and experimental findings of Andani et al. [39] for a thin-walled SMA tube subjected to torsion: **a** temperature changes and **b** shear stress-shear strain response

is also considered as a valuable case study for researchers. Therefore, further investigation is performed on tensile loading of SMA tubes under 0.01 s^{-1} strain rate as illustrated in Fig. 10. Figures 8 9, 10 indicate that the present model is able to predict thermomechanical responses of SMA tubes as well. However, as shown in Figs. 8a, 9a, and 10a, there are differences between the theoretically predicted temperatures and the experimentally measured ones. Two main reasons may cause these differences. First, heat transfer between the SMA component and its grippers exists in practice but is not considered in the numerical simulations conducted in either this research or the reference works. Second, phase transformation does not actually take place homogeneously, and the local phenomena of nucleation and propagation of a phase front cause instantaneous temperature of an SMA part to be different at different locations. Such details are not taken into account in the reported theoretical results. Moreover, depending on the location where the experimental temperatures are measured, the observed amount of error may differ. In Figs. 8b and 9b, where shear stress-strain responses are illustrated, some discrepancies between the numerical and the empirical results may be mainly due to the so-called phenomenon of tension-torsion coupling [44–46] under torsion. Briefly describing, when an SMA specimen is under torsion, axial deformations may occur. Therefore, similar to the response of an anisotropic material, axial stress and strain may be induced too. The extent of such axial deformations depends on several material and geometric parameters [45], which are not reported in the reference experiments since such details have not been the subject of those works. Since tension-torsion coupling is ignored in the reported

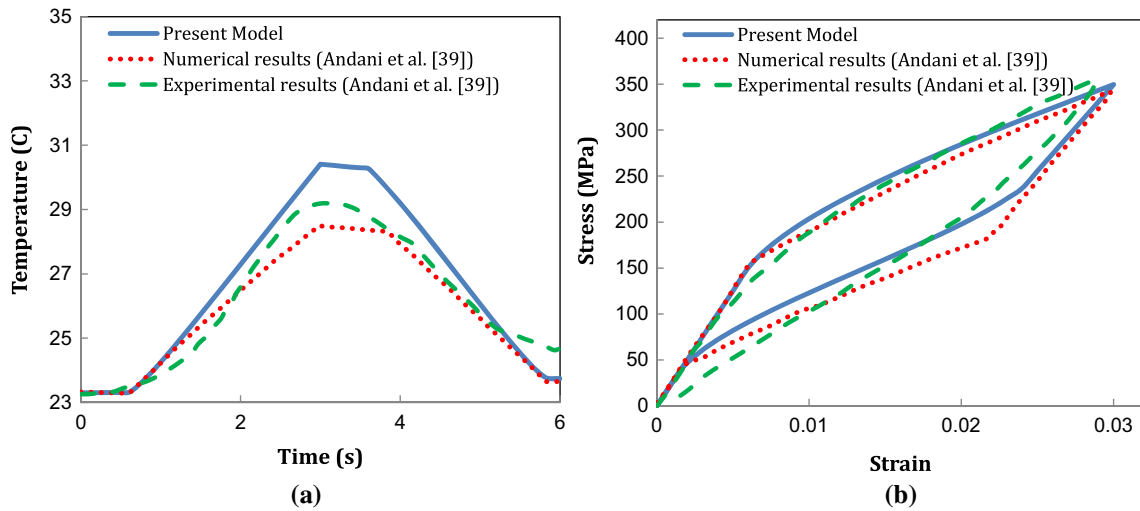


Fig. 10 Numerical and experimental predictions for **a** temperature variations and **b** stress–strain response for an SMA tube subjected to tensile loading

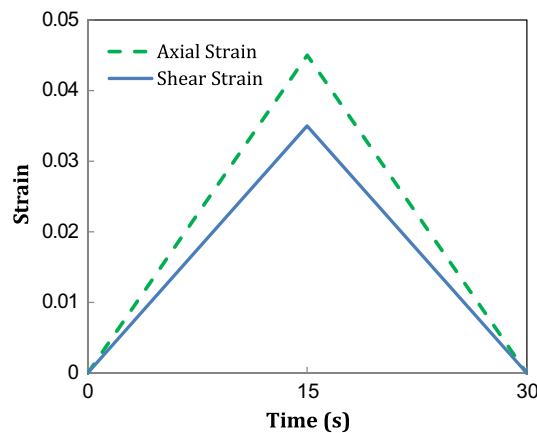


Fig. 11 Proportional strain path used for multiaxial simulation [40]

theoretical responses, the observed errors may arise. In 8.b, 9.b, and 10.b, some residual strain is observed at the end of unloading in the empirical results while the theories predict complete recovery of the induced deformations. Such unrecoverable strains can be minimized (or even diminished) in practice by training the experimental samples.

The next studied case is tension–torsion of an SMA tube in accordance with the work of Andani and Elahinia [40]. The proportional loading/unloading cycle illustrated in Fig. 11 is considered in this case. Shown in Fig. 12 is a comparison between obtained numerical results by the present model and experimental as well as numerical findings of Andani and Elahinia [40] for shear and normal strain rates of 0.0024 s^{-1} , and 0.003 s^{-1} , respectively. The aforementioned tension–torsion coupling is more pronounced in this combined loading and may cause the observed differences between the experimental and theoretical results. The applied von Mises equivalent stress and strain under tension–torsion loading paths have been recommended to be replaced by generalized equivalent stress and strain [44–46], and this promotion can be considered in future works. It is worth noting that conducting a tension–torsion test on an SMA tube has a crucial challenge of applying adequate gripping force so that the axial and torsional degrees of freedom remain independent of each other.

Springs are widely used in common applications of SMAs and, in the case of large applied displacements, experience not only shear stresses but also noticeable normal ones [47]. Simulating the response of an SMA spring under thermal cycling by 1-D numerical models is not as straightforward as mechanical loadings. On the other hand, 2-D/3-D rate-dependent models related to mechanical loadings of SMA springs have been rarely presented in the literature. Thus, employing 3-D fully coupled models implemented by finite element method

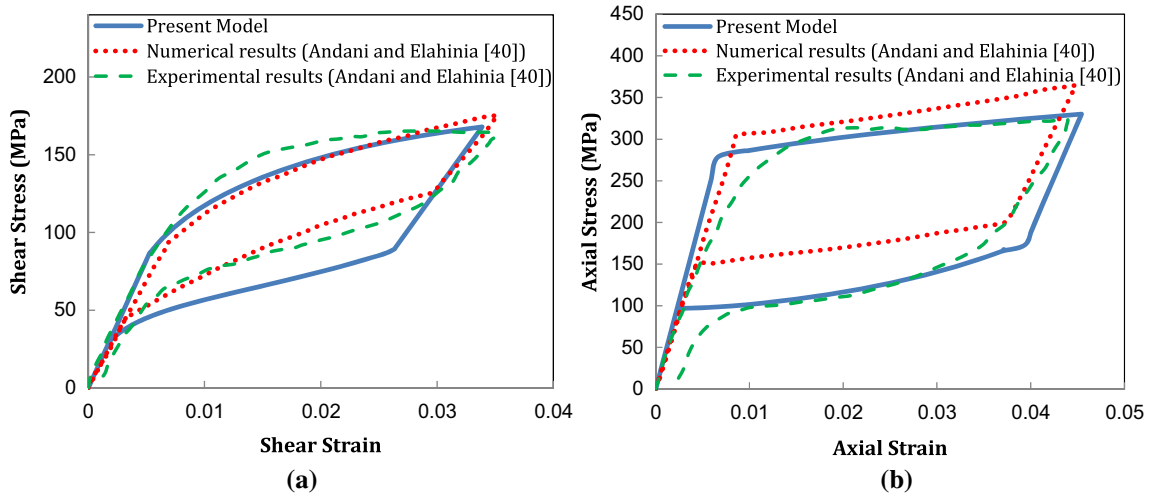


Fig. 12 Comparison between results predicted by the current model and numerical as well as experimental data of Andani and Elahinia [40]: **a** shear stress–shear strain response and **b** axial stress–axial strain response for biaxial loading of a thin-walled SMA tube according to Fig. 11

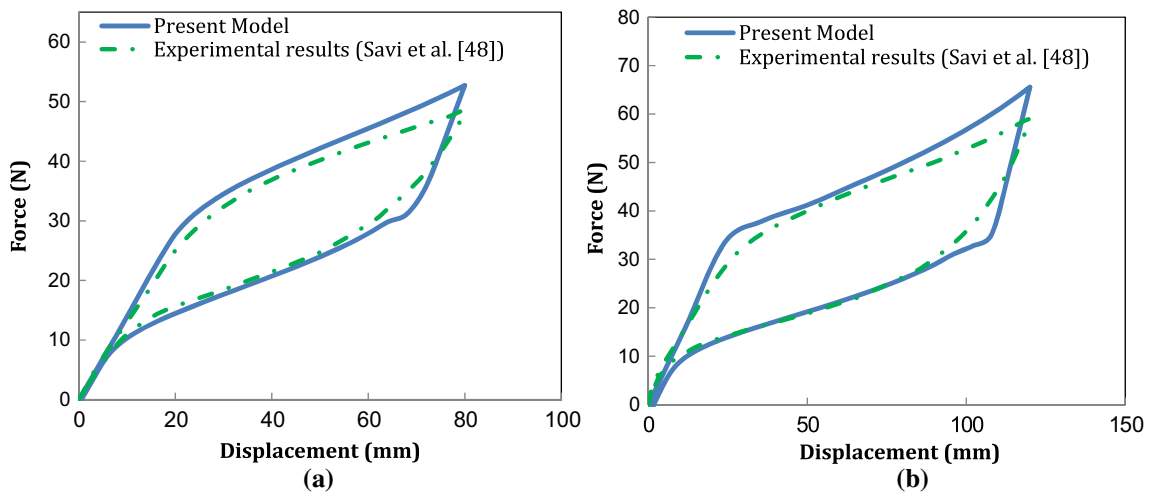


Fig. 13 Comparison between the predicted force–displacement response of a helical spring by the presented model and experimental findings [48]

Table 4 Employed material parameters for finite element simulation of an SMA spring [48]

σ_s^{AM} (MPa)	σ_f^{AM} (MPa)	σ_s^{MA} (MPa)	σ_f^{MA} (MPa)	E (GPa)	ϵ^*
297	772	306	78	46	0.07

plays an important role in studying SMA springs particularly those which are thermally actuated. To study the ability of the proposed model in SMA springs, experimental results of Savi et al. [48] are compared with predicted numerical results by the proposed approach as shown in Fig. 13. The force–displacement response of a spring with the geometrical characteristics of 1.7 mm wire diameter, five active coils, and 13.8 mm spring diameter was investigated at two final displacements of 80 mm and 120 mm by employing material parameters of Table 4. As Fig. 13 shows, maximum errors of 8% and 11% are seen in the calculated forces at the final displacements of 80 mm and 120 mm, respectively.

Since SMA rate-dependent models simultaneously solve the constitutive and thermal equations, heat transfer circumstances strongly influence the temperature variations as well as stress–strain response. Accordingly, different convective heat transfer coefficients comprising infinite h , which is associated with quasi-static con-

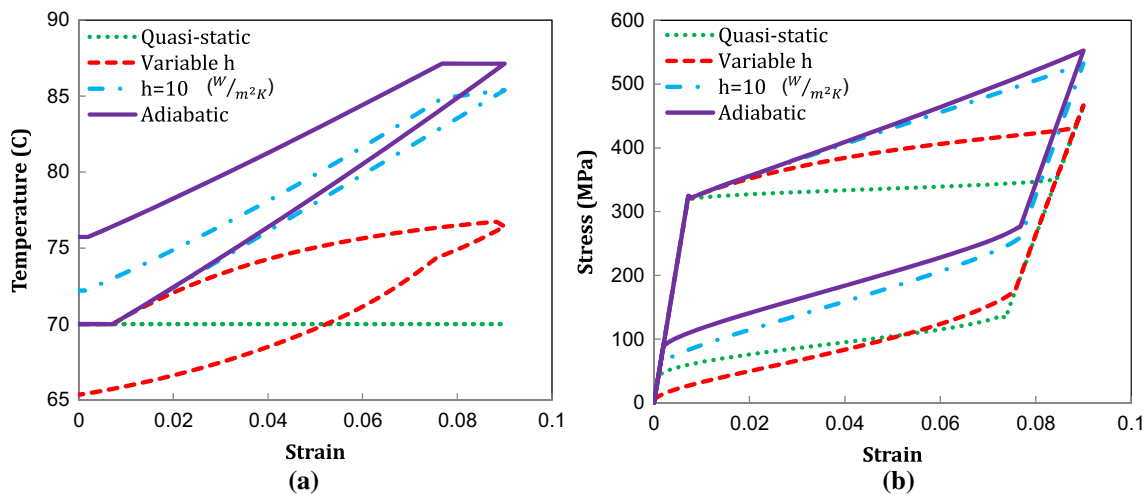


Fig. 14 Effect of different convective heat transfer coefficients on the: **a** temperature–strain response and **b** stress–strain response of SMA wires at the ambient temperature of 70 °C under 0.01 s^{−1} strain rate

dition, temperature-dependent h [49], $h = 10$ (W/m²K), and $h = 0$ (associated to adiabatic condition) are considered to study the effect of heat transfer coefficient on thermomechanical response of an SMA wire. Figure 14 illustrates the temperature–strain and stress–strain responses using the given material parameters in Table 3. As expected, adiabatic conditions suppress heat transfer with ambient so that the temperature at the end of loading reaches the maximum value of 87 °C. On the other hand, for temperature-dependent convective heat transfer coefficient, temperature at the end of cycling is lower than the ambient temperature. As shown in Fig. 14, heat transfer conditions can strongly influence the trend of temperature–stress variations so an appropriate h value for a problem must be chosen depending on the geometry/material parameters and loading/ambient conditions.

As the last case study, capabilities of the model in cyclic loadings of SMA wires under 0.01 s^{−1} strain rate are evaluated in Fig. 15 by utilizing the material parameters of Table 3. As this figure depicts, the temperature–strain and stress–strain responses converge to stabilized curves after a few transient cycles. Simulating the cyclic behavior of an SMA component under a multiaxial loading is useful for the calculation of stabilized dissipated energy and, in turn, prediction of fatigue lifetime. On the other hand, thermal cycling on an SMA component results in functional fatigue, which is also able to be studied by the proposed model.

As can be seen in Figs. 6a, 8a, 9a, 10a, 14a, and 15a, SMA components may experience considerable temperature variations upon loading/unloading depending on loading characteristics, material, geometry, and environment parameters. This temperature variation, which is due to the elastocaloric effect, has been employed in the last years to propose a solid-state refrigerator [50]. With the use of 3-D rate-dependent models, such as the one presented here, elastocaloric effect in SMA refrigerators can be evaluated and optimized to increase efficiency of the system.

5 Conclusions

In this paper, a three-dimensional, fully coupled, rate-dependent model for shape memory alloys was presented. The model was numerically implemented by ABAQUS finite element software through providing a user-defined material subroutine (UMAT). The obtained numerical results by the current model were shown to be in reasonable agreement with available theoretical and empirical data for different cases including tension, torsion, and proportional tension–torsion of prismatic parts as well as axial loading of SMA helical springs. It was illustrated that the presented model is able to simulate the response of an SMA component in quasi-static and rate-dependent circumstances, under thermal as well as 3-D mechanical loadings, not only for pseudoelasticity but also for shape memory effect. Owing to the numerical implementation of the model by ABAQUS, different geometries and boundary conditions, thermomechanical loadings, and convective heat transfer coefficients are able to be investigated by the current approach. The developed UMAT is also able to be employed in finite element analysis of smart structures where an SMA element is applied as an actuator, a damper, or an elastocaloric cooler/heat pump. Moreover, the presented approach provides the capability of studying cyclic

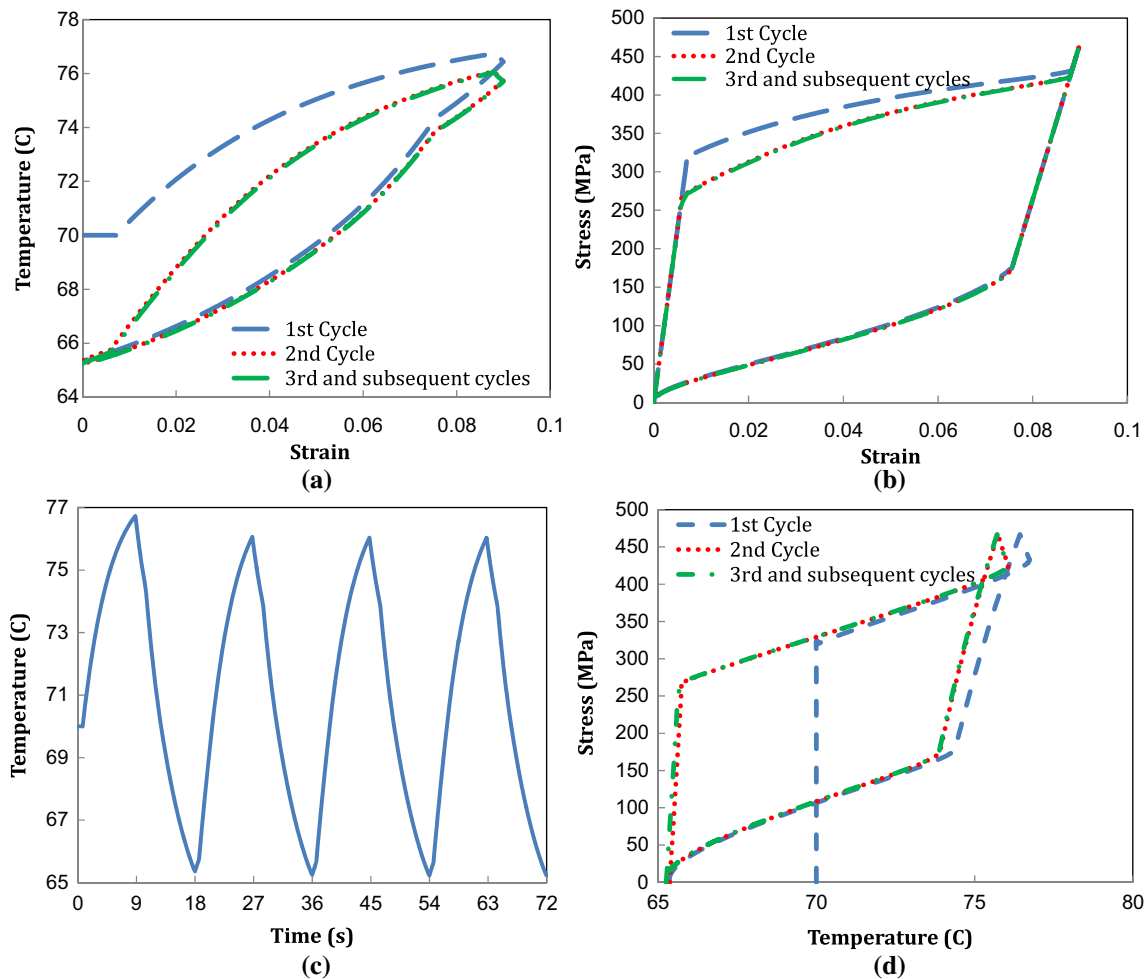


Fig. 15 a Temperature–strain response, b stress–strain response, c temperature–time response, and d stress–temperature response for cyclic mechanical loading of an SMA wire

thermomechanical loadings which makes it beneficial to analyze structural/functional fatigue behavior and to design, evaluate, or optimize SMA components under fatigue loadings. To promote potentials of the presented model, it may be incorporated by nonlocal constitutive equations to capture nucleation and propagation of phase fronts in an SMA. Additionally, generalized equivalent stress and strain should be replaced with the utilized equivalent von Mises ones in this work to provide the ability to consider tension–torsion coupling and the related phenomena especially under nonproportional loadings.

References

1. Jani, J.M., Leary, M., Subic, A., Gibson, M.A.: A review of shape memory alloy research, applications and opportunities. *Mater. Des.* **56**, 1078–1113 (2014)
2. Alessandrini, S., Andraus, U., dell’Isola, F., Porfiri, M.: Piezo-electromechanical (pem) Kirchhoff-Love plates. *Eur. J. Mech. A Solids* **23**(4), 689–702 (2004)
3. Rosi, G., Pouget, J., dell’Isola, F.: Control of sound radiation and transmission by a piezoelectric plate with an optimized resistive electrode. *Eur. J. Mech. A Solids* **29**(5), 859–870 (2010)
4. Giorgio, I., Culla, A., Del Vescovo, D.: Multimode vibration control using several piezoelectric transducers shunted with a multiterminal network. *Arch. Appl. Mech.* **79**(9), 859 (2009)
5. Alessandrini, S., Dell’Isola, F., Frezza, F.: Optimal piezo-electro-mechanical coupling to control plate vibrations. *Int. J. Appl. Electromagn. Mech.* **13**(1–4), 113–120 (2001)

6. Alipour, A., Kadkhodaei, M., Safaei, M.: Design, analysis, and manufacture of a tension-compression self-centering damper based on energy dissipation of pre-stretched superelastic shape memory alloy wires. *J. Intell. Mater. Syst. Struct.* **28**(15), 2129–2139 (2017)
7. Cohades, A., Hostettler, N., Pauchard, M., Plummer, C.J., Michaud, V.: Stitched shape memory alloy wires enhance damage recovery in self-healing fibre-reinforced polymer composites. *Compos. Sci. Technol.* **161**, 22–31 (2018)
8. Barchiesi, E., Spagnuolo, M., Placidi, L.: Mechanical metamaterials: a state of the art. *Math. Mech. Solids* **24**(1), 212–234 (2019)
9. Dell’Isola, F., Seppecher, P., Alibert, J.J., Lekszycki, T., Grygoruk, R., Pawlikowski, M., Steigmann, D., et al.: Pantographic metamaterials: an example of mathematically driven design and of its technological challenges. *Continuum Mech. Thermodyn.* **31**(4), 851–884 (2019)
10. Taheri Andani, M., Haberland, C., Walker, J.M., Karamooz, M., et al.: Achieving biocompatible stiffness in NiTi through additive manufacturing. *J. Intell. Mater. Syst. Struct.* **27**(19), 2661–2671 (2016)
11. Vaiana, N., Sessa, S., Marmo, F., Rosati, L.: A class of uniaxial phenomenological models for simulating hysteretic phenomena in rate-independent mechanical systems and materials. *Nonlinear Dyn.* **93**, 1647–1669 (2018)
12. Cuomo, M.: Forms of the dissipation function for a class of viscoplastic models. *Math. Mech. Complex Syst.* **5**(3), 217–237 (2017)
13. Giorgio, I., Scerrato, D.: Multi-scale concrete model with rate-dependent internal friction. *Eur. J. Environ. Civ. Eng.* **21**(7–8), 821–839 (2017)
14. Eremeyev, V.A., Pietraszkiewicz, W.: The nonlinear theory of elastic shells with phase transitions. *J. Elast.* **74**(1), 67–86 (2004)
15. Pietraszkiewicz, W., Eremeyev, V., Konopińska, V.: Extended non-linear relations of elastic shells undergoing phase transitions. *ZAMM-J. Appl. Math. Mechanics Zeitschrift für Angewandte Mathematik und Mechanik* **87**(2), 150–159 (2007)
16. Eremeyev, V.A., Pietraszkiewicz, W.: Thermomechanics of shells undergoing phase transition. *J. Mech. Phys. Solids* **59**(7), 1395–1412 (2011)
17. Eremeyev, V.A., Pietraszkiewicz, W.: Phase transitions in thermoelastic and thermoviscoelastic shells. *Arch. Mech.* **61**(1), 41–67 (2009)
18. Eremeyev, V.A., Konopińska-Zmysłowska, V.: On the correspondence between two- and three-dimensional Eshelby tensors. *Continuum Mech. Thermodyn.* (2019). <https://doi.org/10.1007/s00161-019-00754-6>
19. Boyd, J.G., Lagoudas, D.C.: A thermodynamical constitutive model for shape memory materials. Part I. The monolithic shape memory alloy. *Int. J. Plast.* **12**(6), 805–842 (1996)
20. Lim, T.J., McDowell, D.L.: Mechanical behavior of an Ni-Ti shape memory alloy under axial-torsional proportional and nonproportional loading. *J. Eng. Mater. Technol.* **121**(1), 9–18 (1999)
21. Peng, X., Yang, Y., Huang, S.: A comprehensive description for shape memory alloys with a two-phase constitutive model. *Int. J. Solids Struct.* **38**(38–39), 6925–6940 (2001)
22. Bouvet, C., Calloch, S., LExcellent, C.: A phenomenological model for pseudoelasticity of shape memory alloys under multiaxial proportional and nonproportional loadings. *Eur. J. Mech. A Solids* **23**(1), 37–61 (2004)
23. Panico, M., Brinson, L.C.: A three-dimensional phenomenological model for martensite reorientation in shape memory alloys. *J. Mech. Phys. Solids* **55**(11), 2491–2511 (2007)
24. Arghavani, J., Auricchio, F., Naghdabadi, R., Reali, A., Sohrabpour, S.: A 3-D phenomenological constitutive model for shape memory alloys under multiaxial loadings. *Int. J. Plast.* **26**(7), 976–991 (2010)
25. Kadkhodaei, M., Salimi, M., Rajapakse, R.K.N.D., Mahzoon, M.: Microplane modelling of shape memory alloys. *Phys. Scr.* **2007**(T129), 329–334 (2007)
26. Ravari, M.K., Kadkhodaei, M., Ghaei, A.: A microplane constitutive model for shape memory alloys considering tension-compression asymmetry. *Smart Mater. Struct.* **24**(7), 075016 (2015)
27. Shirani, M., Mehrabi, R., Andani, M.T., Kadkhodaei, M., Elahinia, M., Andani, M.T.: A modified microplane model using transformation surfaces to consider loading history on phase transition in shape memory alloys. In: *ASME 2014 Conference on Smart Materials, Adaptive Structures and Intelligent Systems*, pp. V001T01A001–V001T01A001, Newport, Rhode Island, USA (2014)
28. Mehrabi, R., Kadkhodaei, M., Ghaei, A.: Numerical implementation of a thermomechanical constitutive model for shape memory alloys using return mapping algorithm and microplane theory. In: *Advanced Materials Research*, vol. 516, pp. 351–354, Switzerland (2012)
29. Zhou, T., Yu, C., Kang, G., Kan, Q.: A new microplane model for non-proportionally multiaxial deformation of shape memory alloys addressing both the martensite transformation and reorientation. *Int. J. Mech. Sci.* **152**, 63–80 (2019)
30. Xue, L., Mu, H., Feng, J.: Thermal mechanical behavior of a functionally graded shape memory alloy cylinder subject to pressure and graded temperature loads. *J. Mater. Res.* **33**(12), 1806–1813 (2018)
31. Auricchio, F., Sacco, E.: Thermo-mechanical modelling of a superelastic shape-memory wire under cyclic stretching-bending loadings. *Int. J. Solids Struct.* **38**, 6123–6145 (2001)
32. Vitiello, A., Giorleo, G., Morace, R.E.: Analysis of thermomechanical behaviour of Nitinol wires with high strain rates. *Smart Mater. Struct.* **14**, 215–221 (2005)
33. Kadkhodaei, M., Rajapakse, R.K.N.D., Mahzoon, M., Salimi, M.: Modeling of the cyclic thermomechanical response of SMA wires at different strain rates. *Smart Mater. Struct.* **16**(6), 2091–2101 (2007)
34. Morin, C., Moumni, Z., Zaki, W.: Thermomechanical coupling in shape memory alloys under cyclic loadings: experimental analysis and constitutive modeling. *Int. J. Plast.* **27**(12), 1959–1980 (2011)
35. Alipour, A., Kadkhodaei, M., Ghaei, A.: Finite element simulation of shape memory alloy wires using a user material subroutine: parametric study on heating rate, conductivity, and heat convection. *J. Intell. Mater. Syst. Struct.* **26**(5), 554–572 (2014)
36. Morin, C., Moumni, Z., Zaki, W.: A constitutive model for shape memory alloys accounting for thermomechanical coupling. *Int. J. Plast.* **27**(5), 748–767 (2011)

37. Mirzaeifar, R., DesRoches, R., Yavari, A.: Analysis of the rate-dependent coupled thermo-mechanical response of shape memory alloy bars and wires in tension. *Continuum Mech. Thermodyn.* **23**(4), 363–385 (2011)
38. Mirzaeifar, R., DesRoches, R., Yavari, A., Gall, K.: Coupled thermo-mechanical analysis of shape memory alloy circular bars in pure torsion. *Int. J. Non-Linear Mech.* **47**(3), 118–128 (2012)
39. Andani, M.T., Alipour, A., Elahinia, M.: Coupled rate-dependent superelastic behavior of shape memory alloy bars induced by combined axial-torsional loading: a semi-analytic modeling. *J. Intell. Mater. Syst. Struct.* **24**(16), 1995–2007 (2013)
40. Andani, M.T., Elahinia, M.: A rate dependent tension-torsion constitutive model for superelastic nitinol under non-proportional loading; a departure from von Mises equivalency. *Smart Mater. Struct.* **23**(1), 015012 (2014)
41. Brinson, L.C.: One-dimensional constitutive behavior of shape memory alloys: thermomechanical derivation with non-constant material functions and redefined martensite internal variable. *J. Intell. Mater. Syst. Struct.* **4**(2), 229–242 (1993)
42. Chung, J.H., Heo, J.S., Lee, J.J.: Implementation strategy for the dual transformation region in the Brinson SMA constitutive model. *Smart Mater. Struct.* **16**(1), N1 (2007)
43. Dassault Systems: Abaqus 6.11-1 Analysis User's Manual. Providence, RI: Dassault Systems (2011)
44. Mehrabi, R., Andani, M.T., Elahinia, M., Kadkhodaei, M.: Anisotropic behavior of superelastic NiTi shape memory alloys; an experimental investigation and constitutive modeling. *Mech. Mater.* **77**, 110–124 (2014)
45. Mehrabi, R., Kadkhodaei, M., Elahinia, M.: Constitutive modeling of tension-torsion coupling and tension-compression asymmetry in NiTi shape memory alloys. *Smart Mater. Struct.* **23**(7), 075021 (2014)
46. Mehrabi, R., Andani, M.T., Kadkhodaei, M., Elahinia, M.: Experimental study of NiTi thin-walled tubes under uniaxial tension, torsion, proportional and non-proportional loadings. *Exp. Mech.* **55**(6), 1151–1164 (2015)
47. Enemark, S., Santos, I.F., Savi, M.A.: Modelling, characterisation and uncertainties of stabilised pseudoelastic shape memory alloy helical springs. *J. Intell. Mater. Syst. Struct.* **27**(20), 2721–2743 (2016)
48. Savi, M.A., Pacheco, P.M.C., Garcia, M.S., Aguiar, R.A., De Souza, L.F.G., Da Hora, R.B.: Nonlinear geometric influence on the mechanical behavior of shape memory alloy helical springs. *Smart Mater. Struct.* **24**(3), 035012 (2015)
49. Shu, S.G., Lagoudas, D.C., Hughes, D., Wen, J.T.: Modeling of a flexible beam actuated by shape memory alloy wires. *Smart Mater. Struct.* **6**(3), 265–277 (1997)
50. Tušek, J., Engelbrecht, K., Eriksen, D., Dall'Olio, S., Tušek, J., Pryds, N.: A regenerative elastocaloric heat pump. *Nat. Energy* **1**(10), 16134 (2016)